Monthly Notices
of the
ROYAL ASTRONOMICAL SOCIETY

MNRAS **461,** 2234–2249 (2016)
Advance Access publication 2016 June 17

doi:10.1093/mnras/stw1448

Orbital and physical parameters of eclipsing binaries from the ASAS catalogue – IX. Spotted pairs with red giants

M. Ratajczak,[1]★ K. G. Hełminiak,[1,2] M. Konacki,[1] A. M. S. Smith,[3] S. K. Kozłowski,[1] N. Espinoza,[4] A. Jordán,[4] R. Brahm,[4] M. Hempel,[4] D. R. Anderson[5] and C. Hellier[5]

[1]*Nicolaus Copernicus Astronomical Center, Department of Astrophysics, ul. Rabiańska 8, PL-87-100 Toruń, Poland*
[2]*Subaru Telescope, National Astronomical Observatory of Japan, 650 North Aohoku Place, Hilo, HI 96720, USA*
[3]*Nicolaus Copernicus Astronomical Center, ul. Bartycka 18, PL-00-716 Warsaw, Poland*
[4]*Instituto de Astrofísica, Pontificia Universidad Católica de Chile, Av. Vicuña Mackenna 4860, Santiago, Chile*
[5]*Astrophysics Group, Lennard-Jones Laboratories, Keele University, Keele, Staffordshire ST5 5BG, UK*

Accepted 2016 June 15. Received 2016 June 14; in original form 2015 January 19

ABSTRACT

We present spectroscopic and photometric solutions for three spotted systems with red giant components. Absolute physical and orbital parameters for these double-lined detached eclipsing binary stars are presented for the first time. These were derived from the *V*-, and *I*-band ASAS and WASP photometry, and new radial velocities calculated from high quality optical spectra we obtained with a wide range of spectrographs and using the two-dimensional cross-correlation technique (TODCOR). All of the investigated systems (ASAS J184949-1518.7, BQ Aqr, and V1207 Cen) show the differential evolutionary phase of their components consisting of a main-sequence star or a subgiant and a red giant, and thus constitute very informative objects in terms of testing stellar evolution models. Additionally, the systems show significant chromospheric activity of both components. They can be also classified as classical RS CVn-type stars. Besides the standard analysis of radial velocities and photometry, we applied spectral disentangling to obtain separate spectra for both components of each analysed system which allowed for a more detailed spectroscopic study. We also compared the properties of red giant stars in binaries that show spots, with those that do not, and found that the activity phenomenon is substantially suppressed for stars with Rossby number higher than ∼1 and radii larger than ∼20 $R_{\odot}$.

Key words: stars: activity – binaries: eclipsing – binaries: spectroscopic – circumstellar matter – stars: fundamental parameters – stars: individual: ASAS J184949-1518.7 – stars: individual: BQ Aqr – stars: individual: V1207 Cen – infrared: stars.

1 INTRODUCTION

The theory of stellar evolution is one of the greatest achievements of astrophysics. However, careful analysis of observations and their comparison with existing models points to some inadequacies and indicates the need to refine certain aspects, such as treatment of convection, or the issue of stellar activity. Widely used stellar evolution models rely on accurate determinations of stellar parameters such as mass, radius, and effective temperature. As mentioned by Torres, Andersen & Gimenéz (2010), only observational data yielding parameters with errors below ∼1–3 per cent provide sufficiently strong constraints that models with inadequate physics can be rejected.

Non-interacting eclipsing binary systems, composed of stars that have evolved as if they were single, are prime targets to retrieve physical parameters with the required accuracy. Very informative examples are systems consisting of evolved stars which have left the main sequence, e.g. red giants and subgiants. Stars belonging to this category and which have parameters known to the required precision (3 per cent or better) are valuable test beds of stellar evolution models during evolutionary phases about which our knowledge is incomplete (approximate treatment of convection and the unsolved problem of convective core overshooting) and which is not well covered with observational data. There are just a dozen well-characterized red giants (e.g. Andersen et al. 1991; Pietrzyński et al. 2013) and just a few of them have been studied in terms of spectral analysis before.

Systems where the components are in different phases of evolution, like AI Phe (e.g. Andersen et al. 1988; Hełminiak et al. 2009)

★ E-mail: milena@ncac.torun.pl

or ASAS-010538 (Ratajczak et al. 2013), are noticeable too. The combination of a main-sequence star with a red giant or subgiant is very useful for empirical verification of stellar evolution models (Lastennet & Valls-Gabaud 2002).

This paper is part of a larger effort aiming to describe an extensive sample of diverse eclipsing binaries from the ASAS catalogue (Hełminiak et al. 2009; Hełminiak & Konacki 2011; Ratajczak et al. 2013; Hełminiak et al. 2014, 2015). We therefore present the first detailed studies of the detached eclipsing binary systems ASAS J184949-1518.7 (hereafter ASAS-184949), BQ Aqr and V1207 Cen. First we describe our targets, then the data collection and analysis, and finally the results we obtained. Section 6 contains the discussion covering evolutionary status of the systems, age and distance determination, as well as the comparison of giant stars in binaries that show spots with those that do not, while Section 7 summarizes the conclusions.

2 TARGETS

The observing strategy includes the selection of detached eclipsing binaries (hereafter DEBs) from the extensive *ASAS Catalogue of Variable Stars* (ACVS; Pojmański 2002) and a spectroscopic campaign to infer the evolutionary status of every component and determine their physical and orbital parameters. The systems were selected on the basis of the following criteria: period $P > 6$ d, change in brightness < 1.1 mag, $V–K > 1$ mag, in order to search for detached, redder systems with components of solar radius or larger. For the purposes of these studies we focused on the systems whose light curves (LCs) showed out-of-eclipse time-varying brightness modulations possibly driven by the activity of the components. Thus the analysed sample includes the binary systems: ASAS-184949, BQ Aqr, and V1207 Cen.

2.1 ASAS J184949-1518.7

ASAS J184949-1518.7 (TYC 6861-523-1, BD-15 5108) is classified as a DEB in the ACVS. Its apparent V magnitude is 10.29 (Høg et al. 2000), and the amplitude of photometric variations in V-band is 0.22 mag. Out-of-eclipse variations in the system LC are visible. No analysis of the system has been presented in the literature so far.

2.2 BQ Aqr

BQ Aqr (ASAS J233609-1628.2, TYC 6403-563-1, GSC 06403-00563, 1SWASP J233608.93-162808.3) was classified as a variable star in 1931 (Hoffmeister 1931) and its apparent V magnitude is 10.61 (Høg et al. 2000), while the ACVS amplitude of photometric variations in V-band is 0.69 mag. The target was identified as a X-ray source in ROSAT All-Sky Survey (Voges et al. 1999) and followed up in spectroscopic survey (Torres et al. 2006) to estimate its spectral type (K0III), although its orbital solution has not been presented in the literature yet.

2.3 V1207 Cen

V1207 Cen (ASAS J142103-3253.2, TYC 7286-1252-1, 1SWASP J142101.68-325248.8) was classified as a variable by Strohmeier (1966). Its apparent V magnitude is 10.69 (Høg et al. 2000), and the amplitude of photometric variations in V-band is 1.02 mag. This target appears in the RAVE catalogue (Kordopatis et al. 2013) but no orbital solution is presented in the literature. Out-of-eclipse variations in the system LC are noticeable.

3 OBSERVATIONS

3.1 Photometric data

3.1.1 ASAS

For the preliminary LC analysis of the studied systems we used ASAS V-band photometry. 570, 395, and 457 measurements were available in the ACVS for ASAS-184949, BQ Aqr, V1207 Cen, respectively. ASAS-184949 I-band photometry (Sitek & Pojmański 2014) yielded an additional 116 data points. The ACVS data on ASAS-184949 span more than 7 yr (2001 Feb 22 to 2008 Jul 24), and almost 9 yr for each of BQ Aqr (2000 Nov 21 to 2009 Jul 16) and V1207 Cen (2000 Dec 23 to 2009 Aug 13).

The LCs of all the systems show significant out-of-eclipse brightness variations related to chromospheric activity and evolving spots. For the purposes of spot-evolution studies we split the data into four subsets representing particular seasons based on the targets' visibility. For ASAS-184949 there are 105, 87, 86, and 161 measurements in Seasons 1–4 for V-band data, respectively. I-band data were split into subsets defined by V-band data seasons. The aforementioned seasons are defined as periods between 2001 Feb 22 and 2002 Dec 20 for Season 1, 2003 Feb 13 and 2004 Jul 4 for Season 2, 2004 Sep 17 and 2006 Jun 25 for Season 3, and 2005 Sep 20 and 2008 Jul 24 for Season 4. The photometric data sets for BQ Aqr and V1207 Cen were extended by WASP measurements, which are described in Section 3.1.2. ACVS data for these systems were used for a preliminary estimation of systemic period P and time of minimum T_0, while the final analysis was applied just for the WASP data.

3.1.2 WASP

Two of our targets, BQ Aqr and V1207 Cen were also observed by the southern instrument of the Wide Angle Search for Planets (WASP; Pollacco et al. 2006), WASP-South. WASP-South is located at the South African Astronomical Observatory (SAAO), near Sutherland, RSA, and consists of eight Canon 200 mm f/1.8 lenses, each equipped with a broad-band filter (400–700 nm), and an Andor 2048 × 2048 e2V CCD camera, on a single robotic mount. BQ Aqr was observed a total of 20 404 times between 2006 May 15 and 2009 Nov 16: 4818, 5838, 5761, and 3987 times in each of the years 2006–2009, which we denote Seasons 1–4, respectively.

V1207 Cen was observed a total of 18 811 times between 2006 May 4 and 2012 Jun 27. In each of the 2006, 2007, and 2008 seasons, this target was observed by a single camera, while in the 2011 and 2012 seasons, the object was monitored by two of the WASP-South cameras. The 2006 and 2007 seasons data were merged and denoted as Season 1 which contains 5164 measurements, while the 2008, 2011, and 2012 seasons are denoted Seasons 2–4, and contain 2493, 5441, and 5713 data points, respectively.

3.2 Spectroscopic data

ASAS-184949, BQ Aqr, and V1207 Cen are double-lined spectroscopic binaries (SB2). In order to measure radial velocities (RVs) of the systems' components, we carried out observations using the 8.2-m Subaru telescope and the High Dispersion Spectrograph (hereafter HDS; $R \sim 60\,000$; Noguchi et al. 2002), the 2.2 m MPG/ESO telescope with its FEROS spectrograph ($R \sim 48\,000$; Kaufer et al. 1999), the 1.5-m CTIO telescope equipped with the CHIRON[1]

[1] Operated by the SMARTS Consortium.

spectrograph (service mode; $R \sim 80\,000$ in slicer mode, $R \sim 25\,000$ in fibre mode; Schwab et al. 2012; Tokovinin et al. 2013), and the 1.2-m Euler telescope with the CORALIE spectrograph ($R \sim 60\,000$; Queloz et al. 2001).

3.2.1 ASAS-184949

We obtained 31 RV measurements for each component of the ASAS-184949 system: 13 from CHIRON-fibre spectra collected in 2012-2013, eight using the CORALIE spectrograph in September 2011 and May 2012, six using the FEROS spectrograph in 2012–2013, and four from two CCD chips (blue and red) on which the spectrum taken by the HDS spectrograph at the Subaru telescope (August 2011) was recorded.

3.2.2 BQ Aqr

We carried out spectroscopic observations of BQ Aqr which yielded 27 RV measurements. Seventeen spectra were obtained using the CHIRON spectrograph in 2011–2013 (13 in fibre mode, 4 in slicer mode), and 10 spectra were taken with the CORALIE spectrograph during observing runs in 2011 and 2012.

3.2.3 V1207 Cen

Nine RVs for V1207 Cen components come from CHIRON-fibre spectra collected in 2013 and 2014.

4 ANALYSIS

4.1 Photometry

ASAS *V*-band photometric data (fluxes and uncertainties calculated with the ASAS data reduction pipeline) were downloaded from the ACVS photometric catalogue. ASAS *I*-band data were taken from ASAS 3 – The Catalogue of Bright Variable Stars in *I*- band South of Declination of $+28^{\circ}$ by Sitek & Pojmański (2014), which contains measurements of brightness given with errors, obtained with the aforementioned ASAS pipeline.

The WASP data were reduced by the WASP reduction pipeline (Pollacco et al. 2006), which produces magnitudes in the 'WASP-*V*' bandpass defined by the Tycho-2 V_t bandpass. Some correlated ('red') noise affecting the photometry (Smith et al. 2006) was removed by use of the SYSREM algorithm of Tamuz, Mazeh & Zucker (2005).

The LCs were cleaned from obvious outliers and split into subsets representing individual seasons in order to investigate the evolution of the spots. We assume that within these seasons the spots do not evolve significantly. A similar approach was used in the case of V1980 Sgr in Ratajczak et al. (2013).

4.2 Radial velocities

4.2.1 Data reduction

As our work covers heterogenous spectroscopic data sets from a wide range of spectrographs, various pipelines were used to reduce and calibrate the data.

(i) CHIRON – pipeline developed at Yale University (Tokovinin et al. 2013). The wavelength calibration was based on the Thorium–Argon lamp exposure taken just before the science exposure with the same spectrograph settings. As the pipeline does not include barycentric velocity and time corrections, we used the IRAF[2] *rvsao.bcvcorr* task for that purpose.

(ii) FEROS and CORALIE – automated pipeline developed at Pontificia Universidad Catolica de Chile, initially for CORALIE (Jordan et al. 2014), then adopted for FEROS. It includes barycentric and continuum corrections. Spectra were taken in a simultaneous Thorium–Argon mode, where one of the fibres observes a target and the other the ThAr lamp.

(iii) HDS – standard IRAF procedures for echelle spectra. The wavelength calibration was done in the standard manner with Thorium–Argon lamp frames taken at the beginning and at the end of observing nights. We used the IRAF *rvsao.bcvcorr* task for barycentric velocity and time corrections.

4.2.2 RVs calculation

Our own implementation of the two dimensional cross-correlation technique (TODCOR; Zucker & Mazeh 1994) was applied in order to calculate RVs of the analysed stars. The method uses as references various synthetic spectra computed with the ATLAS9 and ATLAS12 codes (Kurucz 1992). The formal RV errors were computed from the bootstrap analysis of TODCOR correlation maps created by adding randomly selected single-order maps. To obtain the best fit with reduced $\chi^2 \approx 1$ for our RV data and avoid error underestimation, the formal errors were multiplied by an appropriate factor. We also noted that the RV errors are much larger for the red giant components than for the main-sequence/subgiant stars, mainly due to their faster rotation, likely caused by tidal locking and synchronization.

Due to the wide range of various spectrographs we used, we also fitted an additional parameter, which allows us to compensate for different RV zero-points. Initially, we set the parameter free and then shifted particular sets of data by the obtained difference in RV zero-points. In the case of BQ Aqr measurements we concluded the difference in RV zero-points between spectrographs is insignificant, so the final fits were done with that parameter fixed to 0.

Additionally, we found the difference between primary and secondary centre-of-mass velocities (γ_1 and γ_2) is not negligible, thus we subtracted γ_2 from the secondary RVs and assumed γ_1 as a general system centre-of-mass velocity. There are several possible reasons for the aforementioned shift in velocities among which template mismatch during TODCOR RVs calculations is the most significant one. Following Torres, Claret & Young (2009) we stress that the difference may be also caused by presence of spots on one or both components which can affect the velocities, or large scale convective motions that could be different in two stars.

4.3 Modelling

In our analysis we adopted the primary component as the star being eclipsed during the deeper (primary) eclipse (i.e. hotter) and defined T_0 as the time of the deeper eclipse.

ASAS and WASP photometry was combined with the RV measurements to derive absolute orbital and physical parameters of the studied systems. The modelling procedure we used was described

[2] IRAF is written and supported by the IRAF programming group at the National Optical Astronomy Observatories (NOAO) in Tucson, AZ. NOAO is operated by the Association of Universities for Research in Astronomy (AURA), Inc. under cooperative agreement with the National Science Foundation. http://iraf.noao.edu/

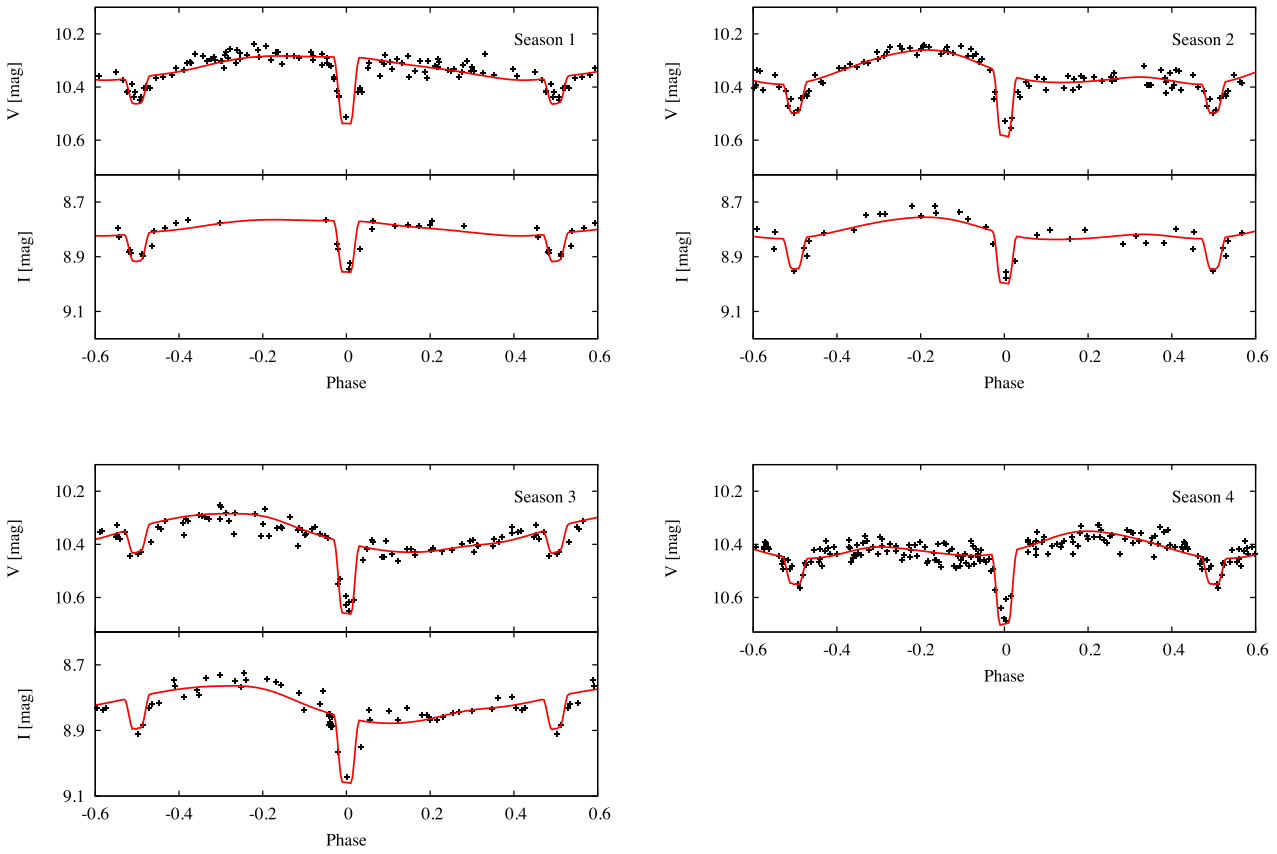

Figure 1. *V*- and *I*-band ASAS-184949 LCs for four seasons with the best-fitting model. Chromospheric activity explained by the existence of evolving spots on the system components influences the LCs significantly. There is no *I*-band data available for Season 4.

in detail in our previous publication – Ratajczak et al. (2013). It applies the following codes: V2FIT which fits a double-Keplerian RV orbit and minimizes the χ^2 function with a Levenberg-Marquardt algorithm (RVs solution), JKTEBOP (v28; LC modelling, Southworth, Maxted & Smalley 2004a; Southworth et al. 2004b), PHOEBE (v0.31a; *Physics Of Eclipsing Binaries*; Prša & Zwitter 2005), and JKTABSDIM (absolute values of the parameters with their uncertainties, Southworth et al. 2004a,b). At the beginning of our analysis we found orbits consistent with circular for every system, thus we kept the eccentricity fixed at 0 further on. Values of rotational velocity were calculated under the assumption of tidal locking and synchronization, which was based on the comparison of circularization and synchronization time-scales (e $\sim$ 0 and $t_{\rm synch} < t_{\rm circ}$ for all systems). The tidal locking assumption is consistent with our initial SME (*Spectroscopy Made Easy*; see further Sections) $v_{\rm rot}$ estimations and with the fact that wider spectral lines belong to larger components. Assuming synchronous rotation and circular orbits for eclipsing binaries (sin i $\approx$ 1) we presume spin-orbit alignment, so $i_{\rm rot} = i_{\rm orb}$, thus $v_{\rm rot} \simeq v_{\rm rot} \sin i$.

Photometric scale factors were adjusted in PHOEBE, and gravitational darkening coefficients were set at the value of $\beta = 0.32$ (Lucy 1967). Limb darkening was modelled using the logarithmic law of Klinglesmith & Sobieski (1970), with the values of coefficients taken from the van Hamme (1993) tables, while surface albedo values were assumed to be the default values from PHOEBE. The analysis showed there is no third light influence.

The mass ratio of the components obtained by applying V2FIT was fixed in our LC modelling. We noticed a non-uniform brightness outside the eclipses, which hindered finding a consistent solution in JKTEBOP, so we used this mostly for correcting the ASAS time of minimum T_0 and the period P. Splitting the photometric data into subsets representing seasons allowed us to study the evolution of spots on the systems' components. The LC for every season was treated as a separate set of data in PHOEBE for which the solution was found adjusting the semimajor axis a, inclination i, effective temperatures $T_{\rm eff}$, luminosity levels, and gravitational potentials Ω, not including stellar spots in a model. The systemic velocity γ_1 and mass ratio were fixed in PHOEBE modelling with the values obtained with V2FIT. Then one season (hereafter base season) was chosen on the basis of the largest data phase coverage and the least-significant spots influence, for which the spots analysis was carried out (for ASAS-184949 and BQ Aqr that was Season 1, for V1207 Cen – Season 4). We kept the same number of spots on a given component as for the base season in other seasons, but we adjusted the spots' radii, temperatures and locations, to find stellar parameters for each season. Final values of the systems' a, i, and potentials were adopted as weighted means of these quantities from different seasons. The first estimation of the brighter component effective temperature was based on the colour-temperature calibration (Worthey & Lee 2011) using TYCHO-2 colours (Høg et al. 2000), but for the final analysis we used component temperatures obtained by performing spectral analysis using SME (described in Section 4.3.1). *I*-band data were fitted simultaneously with *V*-band data sets during the PHOEBE modelling.

The solutions obtained for the photometric measurements are presented in Figs 1–3. RV curves for ASAS-184949, BQ Aqr, and V1207 Cen are presented in Fig. 4. The mean formal errors of

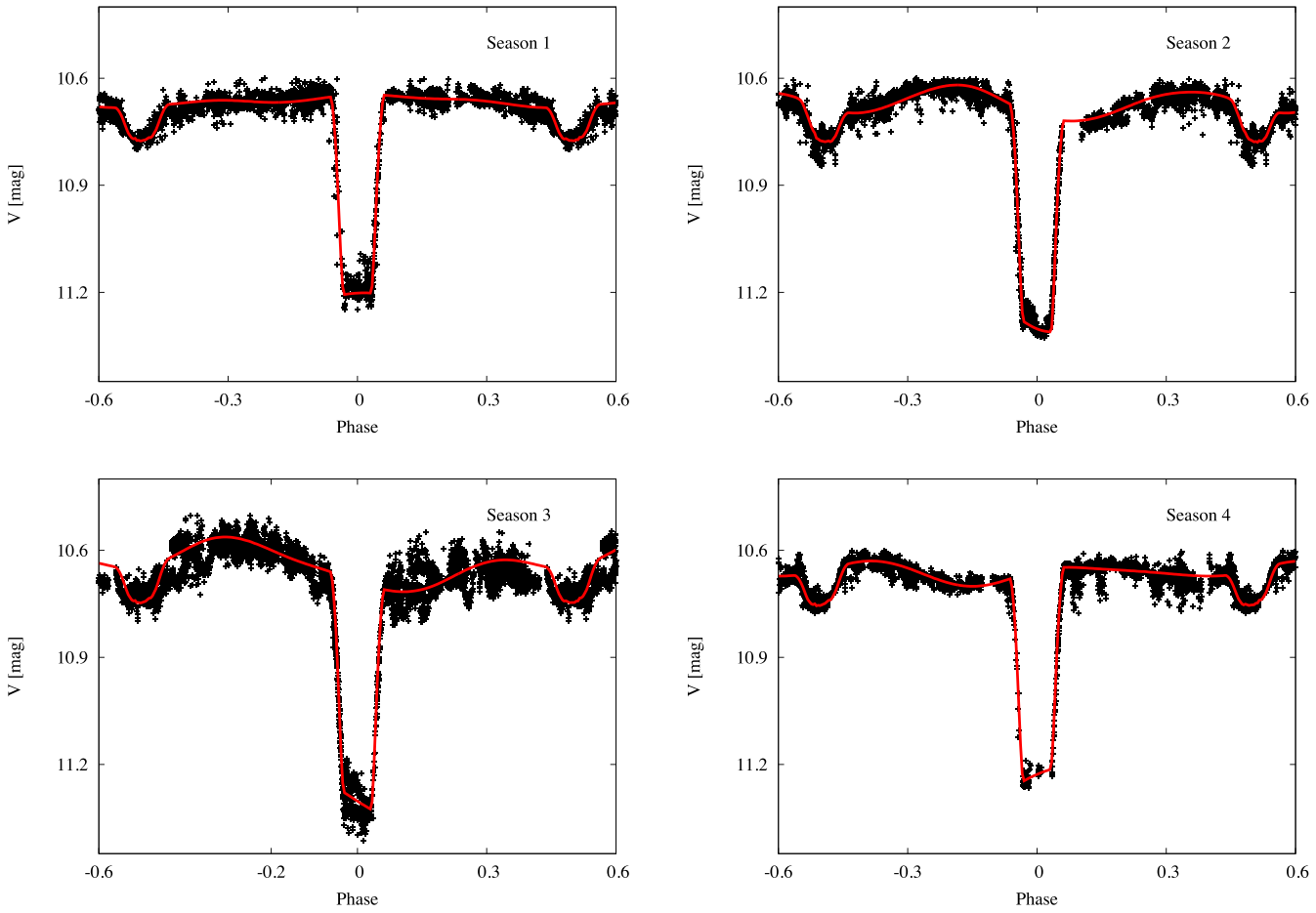

Figure 2. WASP BQ Aqr LCs for four seasons with the best-fitting model. Chromospheric activity explained by the existence of evolving spots on the system's components influences the LCs significantly.

photometric and RVs measurements, RMS of orbital fitting, and multiplicative factors for analysed systems are presented in Table 1.

4.3.1 *Spectral analysis*

For all systems, the phase coverage of the spectroscopic observations from the same spectrograph (CHIRON), taken in the same mode (here: fibre mode) was sufficient to disentangle the components spectra. The spectral disentangling technique (Bagnuolo & Gies 1991; Konacki et al. 2010) was used to extract the individual contributions of both stars to the composite spectra and reconstruct the spectra of each component. It has been proven (Ilijic et al. 2004) that in the case of time-independent component fluxes, spectral disentangling can be performed assuming equal fluxes of the components, and the resulting spectra can be renormalized afterwards. The two separate spectra obtained in this way were scaled by their brightness ratio (hereafter *BR*, defined as primary over secondary brightness ratio) and used for individual studies of every star. Spectral analysis was performed leading to a description of the stellar atmospheres. As significant brightness modulations due to the spots made estimation of *BR* of the systems components troublesome, we adopted the values taken from the TODCOR analysis ($BR_{\rm A184949} = 0.70$, $BR_{\rm BQAqr} = 0.67$, $BR_{\rm V1207Cen} = 0.72$). For detailed spectral analysis we used the software package Spectroscopy Made Easy (hereafter SME, Valenti & Piskunov 1996; Valenti, Piskunov & Johns-Krull 1998).

Following the claim presented in the work of Valenti & Fischer (2005) that line blending becomes more severe in the blue and in cooler stars, making continuum placement and derived parameters less accurate, we analysed only 7 rows (over 38) of the spectra covering the wavelength region from 5927 to 6399 Å. We used the list obtained from the Vienna Atomic Line Database (VALD; Piskunov et al. 1995; Kupka et al. 1999) as the atomic line data with the initial values described by Valenti & Fischer (2005) and Kurucz (1992) model atmospheres.

The spectral synthesis yielded effective temperatures and metallicities for both components of the analysed systems. Keeping the values of log g that we determined in the first stage of the PHOEBE analysis, rotational velocities calculated under the assumption of tidal locking (which were consistent with preliminary spectral analysis results), and solar abundances pattern fixed (Grevesse, Asplund & Sauval 2007), we fitted for $T_{\rm eff}$ and $[M/H]$. As starting values, we used the temperatures we adopted from PHOEBE analysis (brighter component effective temperature based on the colour-temperature calibration from Worthey & Lee 2011) and solar metallicity. Calculations were made for each of seven spectral orders, before finally averaging the results. The variance between different orders was taken as the uncertainty of every parameter.

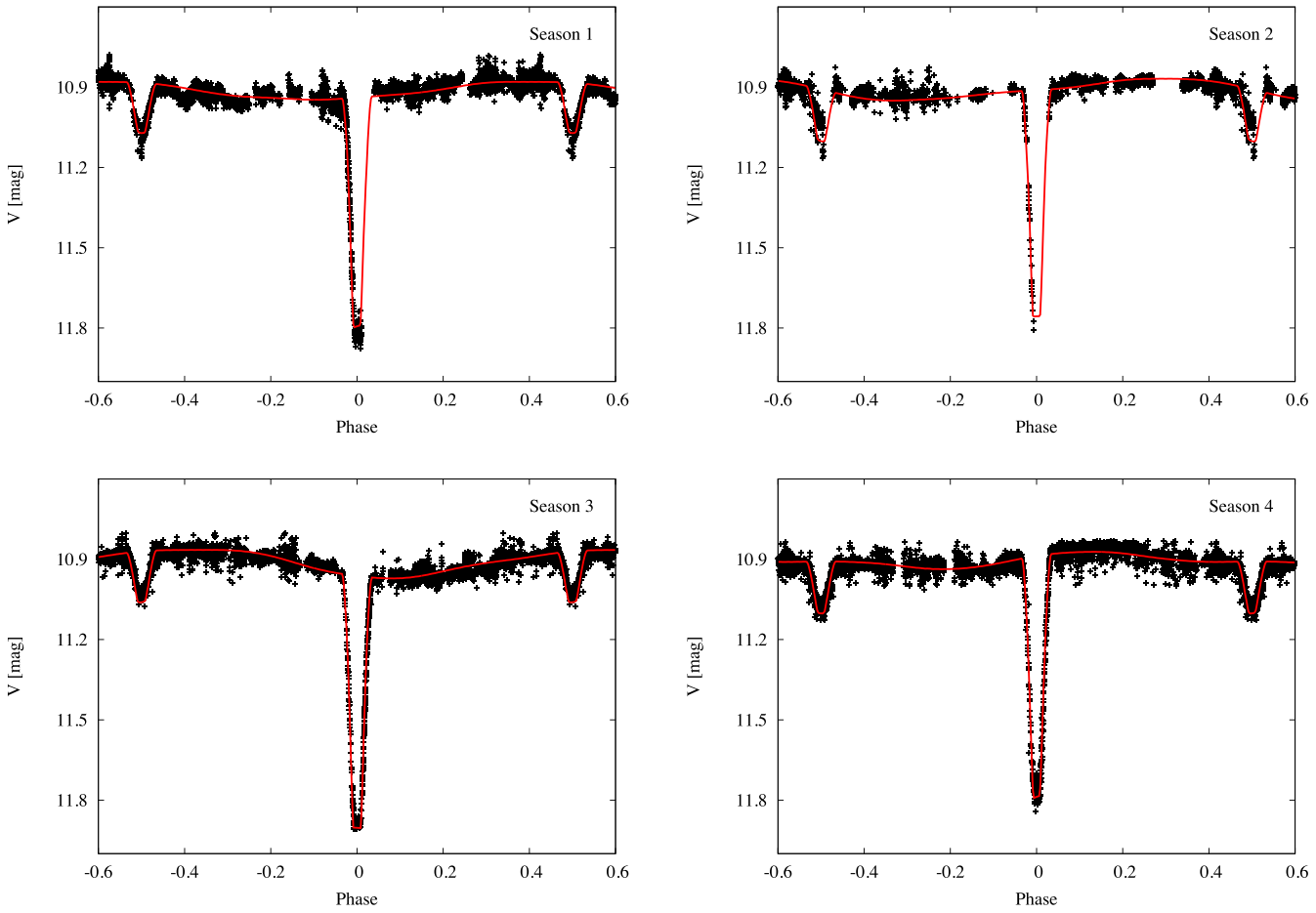

Figure 3. WASP V1207 Cen LCs for four seasons with the best-fitting model. Chromospheric activity explained by the existence of evolving spots on the system's components influences the LCs significantly.

5 RESULTS

The physical and orbital parameters of ASAS-184949, BQ Aqr, and V1207 Cen with their 1σ uncertainties are presented in Table 2. Radii are given in $R_\odot$ units, as well as fractions of Roche limit (Roche radius, $R_{\rm Roche}$). The Roche radius is defined as $R_{\rm Roche}/a = 0.49q^{2/3}/[0.6q^{2/3} + \ln(1 + q^{1/3})]$ (Eggleton 1983) where a is the semimajor axis and q is the mass ratio. Effective temperatures and metallicities are based on the spectral analysis we performed using SME. In order to find distances to the investigated systems we estimated reddening using maps of dust IR emission by Schlegel, Finkbeiner & Davis (1998) recalibrated by Schlafly & Finkbeiner (2011) and then used bolometric corrections by Bessell, Castelli & Plez (1998) to convert bolometric magnitudes into absolute visual magnitudes.

5.1 ASAS-184949

The components' masses are 1.91 $M_\odot$ and 2.19 $M_\odot$, while the radii are 3.0 $R_\odot$ and 9.0 $R_\odot$ for the primary and secondary, respectively. The uncertainties in masses reach 3 per cent and 2 per cent. Unfortunately the quality of the photometric data (just ASAS photometry) and LC modulation makes the determination of radii imprecise, with uncertainties of 22 per cent and 40 per cent.

Strong variability of Hα (6 563 Å) line and emission in its spectral region was detected for ASAS-184949 in HDS spectra. Additionally we noticed emission in Ca II K (3 934 Å), and Ca II H (3 969 Å) lines in FEROS spectra (Fig. 5). Such features can be indicators of an active chromosphere for late-type stars (Strassmeier et al. 1993), and thus the presence of spots on the stellar surfaces which cause significant brightness modulations. The PHOEBE spots analysis resulted in a model with two spots – one located on a primary, the second on the secondary component.

Effective temperatures and metallicities were determined by applying SME to the disentangled spectra and yielded $T_1 = 5560 \pm 400$ K, $T_2 = 4560 \pm 120$ K, $[M/H]_1 = -0.41 \pm 0.26$, and $[M/H]_2 = 0.35 \pm 0.26$ (hereafter solution A). The inconsistency we found in the metallicity of the two components led us to an alternative solution (resulting with $T_1 = 6630 \pm 320$ K and system $[M/H]$ of 0.35) which is described in Section 6.1 (hereafter solution B). The distances we derived are $d_{1849494} = 496 \pm 129$ and 508 ± 133 pc for the solutions A and B, respectively.

The resulting RMS of the residuals to the RV fits are 1.3 km s^{-1} and 2.4 km s^{-1} for the primary and secondary components, respectively. The average photometric error is 0.03 mag (V-band) and 0.07 (I-band).

5.2 BQ Aqr

BQ Aqr components' masses are 1.49 $M_\odot$ and 1.59 $M_\odot$, while the radii are 2.07 $R_\odot$ and 6.53 $R_\odot$ for the primary and secondary, respectively. The masses are determined with a precision of 1 and

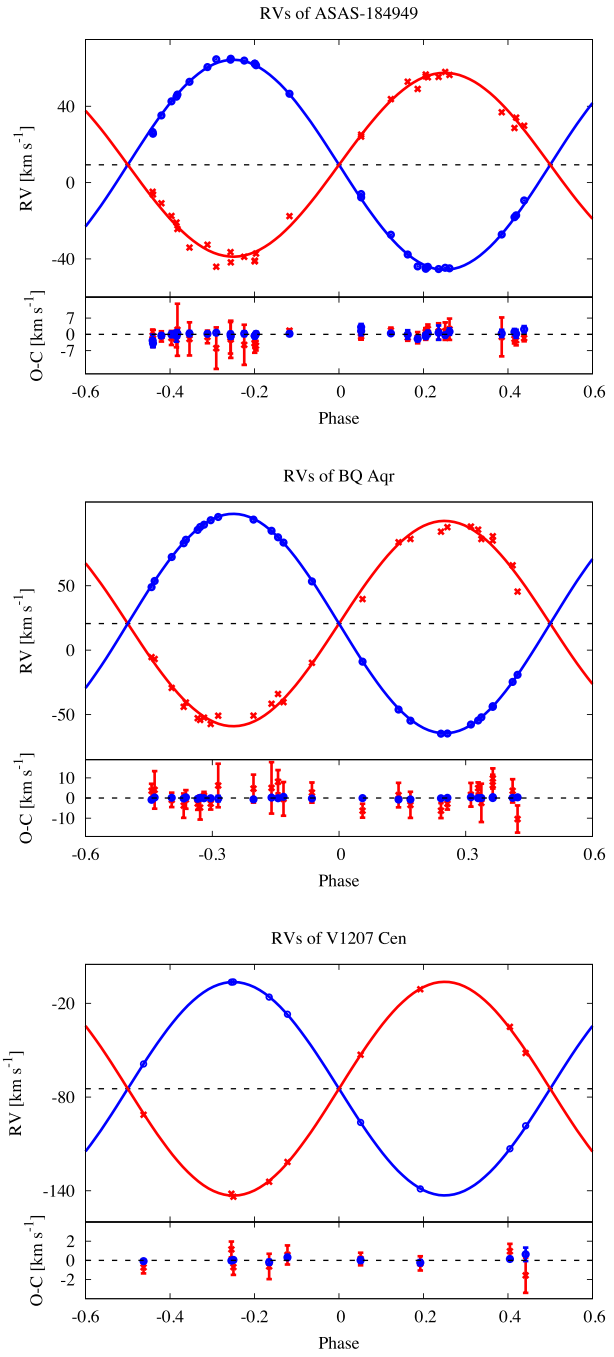

Figure 4. The observed RVs of ASAS-184949, BQ Aqr, and V1207 Cen with their best-fitting Keplerian models and O-Cs with corresponding uncertainties. Circles represent measurements of the primary and crosses measurements of the secondary.

3 per cent and uncertainties in the radii reach 1 per cent for the primary and 4 per cent for the secondary.

As the Ca II K and H region is beyond the CORALIE and CHIRON spectral ranges, we looked at the Balmer lines, but no clear emission was detected. Although no evident traces of chromospheric activity were found in any spectra, the existence of spots on the secondary component was noticeable in the shape of a cross-correlation function. Thus we applied spots to the LC analysis and found a model with three spots (one on the primary, two on the secondary) as the most accurate one.

Effective temperatures determined from the spectral analysis are 6260 ± 240 K for the primary, and 4490 ± 230 K for the secondary, and the metallicities we derived are of $[M/H]_1 = 0.46 \pm 0.22$, and $[M/H]_2 = 0.12 \pm 0.11$. For further analysis we decided to assume the system metallicity as the secondary metallicity value, $[M/H] = 0.12$, because evolutionary tracks calculated for both the primary's metallicity, and the mean of the metallicity values obtained in SME for both components, do not have fitted parameters determined for both components. Adopting $[M/H] = 0.12$, we performed SME spectral analysis obtaining a new value of effective temperature for the primary $T_1 = 6390 \pm 230$ K. The derived distance to the system is $d_{\rm BQAqr} = 617 \pm 75$ pc.

The resulting RMS in the residuals of the fits to the RVs are 0.4 km s^{-1} and 4.9 km s^{-1} for the primary and secondary components, respectively. The average photometric error is 0.16 mag (ASAS) and 0.07 (WASP).

5.3 V1207 Cen

The component masses we obtained are almost equal of 1.13 $M_\odot$ with 1 per cent uncertainties. The radii of the system's components are 1.92 $R_\odot$ for the primary, and 3.00 $R_\odot$ for the secondary. The uncertainties reach 1–3 per cent.

We noted strong variability in the secondary Hα line, including emission in some of the spectra. Other activity indicators, like emission in the Ca II K and H region are beyond CHIRON's spectral range. PHOEBE was used to find the best-fitting model with spots for the system (one big spot on the secondary, and a small one on the primary).

Effective temperatures and metallicities determined from disentangled spectra using SME are $T_1 = 5780 \pm 230$ K, $T_2 = 4560 \pm 160$ K, $[M/H]_1 = -0.16 \pm 0.15$, and $[M/H]_2 = -0.45 \pm 0.11$. Evolutionary tracks calculated either using the primary value or the mean of metallicities showed poor agreement to fitted parameters for both components. The secondary value of $[M/H] = -0.45$ was therefore chosen for further analysis. We found the effective temperature estimation to be in disagreement with the models, so we adopted an alternative solution with $T_1 = 6340$ K and $T_2 = 5000$ K (see Section 6.1) as the final one. We stress that, despite the components having nearly equal masses, the temperatures must be very different, because the LC eclipses show very unequal depths.

The resulting RMS in the residuals of the fits to the RVs are 0.3 km s^{-1} and 0.9 km s^{-1} for the primary and secondary components, respectively. The average photometric error is 0.15 mag (for both ASAS and WASP data). The derived distance is of $d_{\rm V1207Cen} = 447 \pm 31$ pc.

6 DISCUSSION

6.1 Age and evolutionary status

To check the evolutionary status of the stars the Yonsei-Yale (hereafter YY, Yi et al. 2001) evolutionary tracks for α-enhancement of 0 were applied. As there is no mass-loss on the red giant branch assumed in YY models, we estimated the mass-loss using a new formulation of Reimers' Law from Schroder & Cuntz (2005) and found it to be negligible, at least up to the point specifically reached by the giants under scrutiny, thus the application of YY tracks is justified.

Assuming that the system components are coeval and have the same metallicity, we faced the problem of inconsistent metallicity determination for ASAS-184949 ($[M/H]_1 = -0.41$,

Table 1. Mean formal errors of photometric ($\bar{\sigma}_{LC}$) and RVs ($\bar{\sigma}_{RV}$) measurements, RMS of orbital fitting (RMS_{RV}), and multiplicative factors (MF_{RV}) for analysed systems. A-V stands for ASAS-*V* band, A-I – ASAS-*I*, and W – WASP data.

Parameter	ASAS-184949	BQ Aqr	V1207 Cen
$\bar{\sigma}_{LC}$[mag]	0.03 (A-V), 0.07 (A-I)	0.16 (A-V), 0.07 (W)	0.15 (A-V), 0.15 (W)
$\bar{\sigma}_{RV1}$[kms^{-1}]	0.3	0.3	0.1
RMS_{RV1}[kms^{-1}]	1.3	0.4	0.3
MF_{RV1}	4.0	1.7	1.9
$\bar{\sigma}_{RV2}$[kms^{-1}]	0.9	1.3	0.5
RMS_{RV2}[kms^{-1}]	2.4	4.9	0.9
MF_{RV2}	4.0	4.6	1.9

Table 2. Orbital and physical parameters of ASAS-184949, BQ Aqr, and V1207 Cen. Values of effective temperatures T_{eff} and metallicities $[M/H]$ are taken from spectral analyses of disentangled spectra. The values after the slash of T_{eff}, $[M/H]$, L, and M_{bol} for the primary component of ASAS-184949 and BQ Aqr, and both components of V1207 Cen describe alternative solutions for the systems (see Section 6.1).

Parameter	ASAS-184949	BQ Aqr	V1207 Cen
P [d]	35.7091 ± 0.0011	6.620 5062 ± 0.000 0021	8.536 5711 ± 0.000 0011
T_0 [JD-2450000]	2063.214 ± 0.022	1885.443 ± 0.007	1906. 0056 ± 0.0025
K_1 [km s^{-1}]	55.02 ± 0.27	85.18 ± 0.09	68.5 ± 0.4
K_2 [km s^{-1}]	48.2 ± 0.6	79.7 ± 1.1	68.33 ± 0.11
γ_1 [km s^{-1}]	9.3 ± 0.5	20.6 ± 1.8	−74.65 ± 0.09
γ_2 [km s^{-1}]	−3.8 ± 0.6	−1.5 ± 1.9	1.15 ± 0.29
e	0.0 fixed	0.0 fixed	0.0 fixed
i	85.7 ± 1.9	89.5 ± 0.5	88.6 ± 0.5
a [$R_\odot$]	72.69 ± 0.19	21.66 ± 0.08	23.08 ± 0.05
M_1 [$M_\odot$]	1.91 ± 0.05	1.49 ± 0.04	1.132 ± 0.008
M_2 [$M_\odot$]	2.19 ± 0.04	1.588 ± 0.021	1.134 ± 0.013
R_1 [$R_\odot$]	3.0 ± 0.7	2.072 ± 0.014	1.92 ± 0.06
R_2 [$R_\odot$]	9.0 ± 3.0	6.53 ± 0.28	3.003 ± 0.026
log g_1 [cm s^{-1}]	3.76 ± 0.19	3.977 ± 0.006	3.924 ± 0.026
log g_2 [cm s^{-1}]	2.8 ± 0.4	3.01 ± 0.04	3.537 ± 0.011
v_{rot1} [km s^{-1}]	4.3 ± 0.9	15.83 ± 0.11	11.4 ± 0.3
v_{rot2} [km s^{-1}]	13.0 ± 5.0	49.9 ± 2.6	17.79 ± 0.21
T_{eff1} [K]	5560/6630 ± 400/320	6260/6390 ± 240/230	5780/6340 ± 230
T_{eff2} [K]	4560 ± 120	4490 ± 230	4560/5000 ± 160
$[M/H]_1$	−0.41/0.35 ± 0.26/0.22 (fixed)	0.46/0.12 ± 0.22/0.11 (fixed)	−0.16/-0.45 ± 0.15/0.11 (fixed)
$[M/H]_2$	0.35 ± 0.22	0.12 ± 0.11	−0.45 ± 0.11
log L_1 [$L_\odot$]	0.89/1.20 ± 0.23/0.21	0.77/0.80 ± 0.06/0.06	0.51/0.73 ± 0.06/0.07
log L_2 [$L_\odot$]	1.54 ± 0.38	1.19 ± 0.09	0.57/0.71 ± 0.06/0.06
M_{bol1} [mag]	2.5/1.7 ± 0.6/0.5	2.81/2.72 ± 0.16/0.15	3.47/2.93 ± 0.14/0.16
M_{bol2} [mag]	0.9 ± 0.9	1.76 ± 0.23	3.34/2.98 ± 0.14/0.15
R_1/R_{Roche}	0.11	0.26	0.21
R_2/R_{Roche}	0.33	0.79	0.34

$[M/H]_2 = 0.35$). To test which value is more reliable, tracks for both values were interpolated. Tracks calculated for $[M/H] = -0.41$ (primary metallicity obtained applying SME) do not fit the derived parameters (hereafter solution A), unlike the more reliable tracks obtained by applying $[M/H] = 0.35$ (see left-hand panel of Fig. 6), thus we assumed this value as the proper one. As a next step, we performed an SME analysis keeping the metallicity value $[M/H] = 0.35$ fixed and obtained new values of T_{eff} for the primary. An alternative solution (hereafter solution B) based on the newly computed value (new values of T_{eff1}, L_1, M_{bol1} with errors) is described in Table 2 after the slash. Both solutions with corresponding evolutionary tracks and isochrones are presented in Fig. 6. The resulted evolutionary tracks for the more credible solution B indicate that the primary component is leaving the main-sequence or is in a subgiant phase, while the secondary is already on the red giant branch.

The system age estimation was based on fitting the isochrones from three models: Yonsei-Yale (YY), PARSEC (the PAdova & TRieste Stellar Evolution Code, Bressan et al. 2012), and Dartmouth (Dotter et al. 2007) to the data from both solutions (A and B). Isochrones calculated for $[M/H] = 0.35$ presented on three planes (M_{bol} – mass, log T_{eff} – mass, log g – mass) and shown in Fig. 7 favour the solution B (with $T_{eff1} = 6630$ K) and imply a system age of 1 Gyr.

Evolutionary tracks calculated for the masses of the BQ Aqr components and the system metallicity $[M/H] = 0.12$ (presented in the upper panel of Fig. 8) also imply that the components of the system have different evolutionary phases – the primary is a main-sequence star, while the secondary is a red giant. YY, PARSEC, and Dartmouth isochrones (right-hand panel of Fig. 8) interpolated for $[M/H] = 0.12$ and ages of 2.65, 2.5, and 2.5 Gyr respectively fit the system parameters, yielding an estimated system age of 2.5–2.65 Gyr. Values of L and M_{bol} presented in Fig. 8 were obtained by assuming the system metallicity as $[M/H] = 0.12$ and $T_1 = 6390$ K.

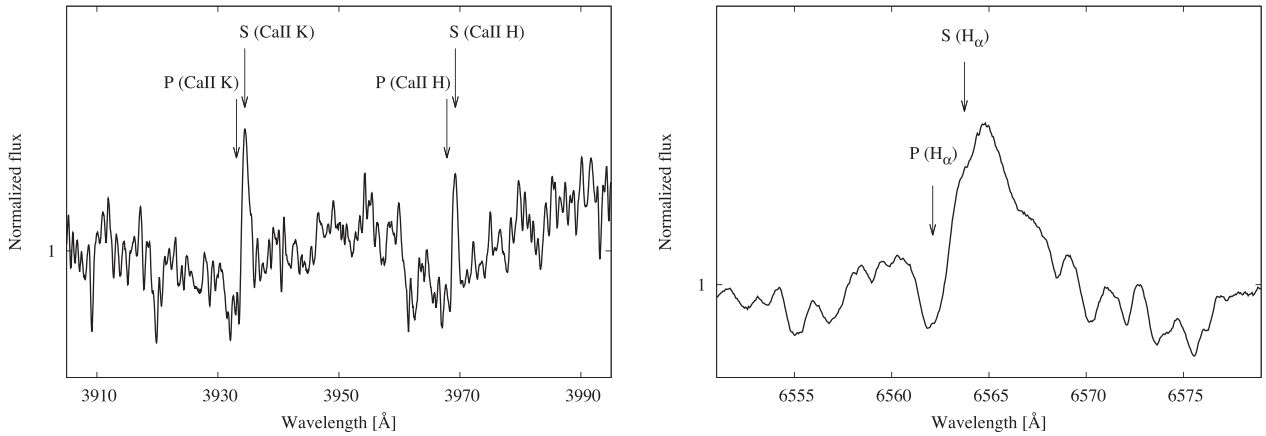

Figure 5. Regions of Ca II H and K (left-hand panel), and Hα (right-hand panel) of continuum normalized FEROS spectra of ASAS-184949. Primary star features are labelled with P, and secondary star features with S, the arrows correspond to RVs of each component inferred from the orbital solution. Emission in secondary star features is significant. The left-hand panel represents a spectrum from 2013 May 16 ($RV_1 = -49.2$ km s^{-1}, $RV_2 = 56.5$ km s^{-1}), and the right-hand panel from 2012 Jun 24 ($RV_1 = -31.8$ km s^{-1}, $RV_2 = 42.2$ km s^{-1}). Spectra were smoothed with a 10-pixel boxcar.

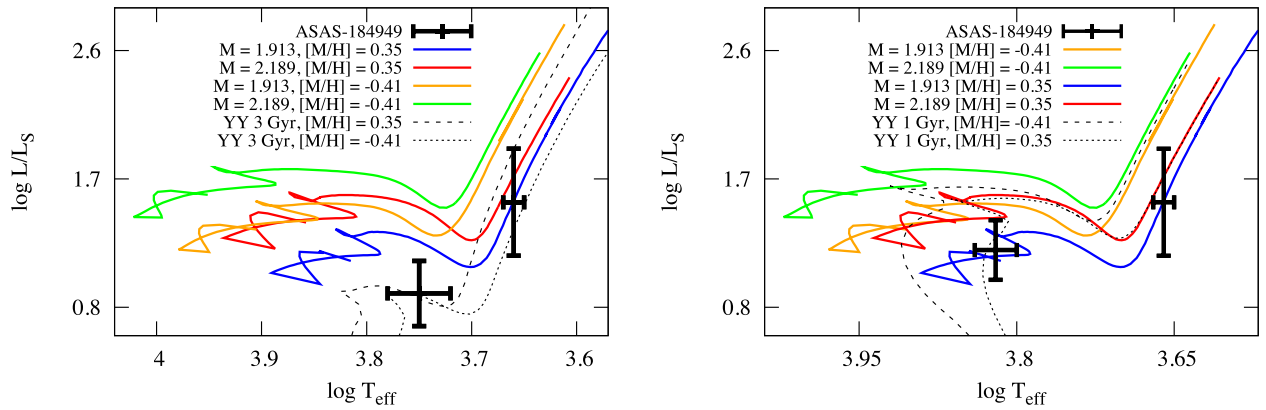

Figure 6. Two parameters solutions (left-hand panel: solution A – $T_{\rm eff1} = 5560$; right-hand panel: solution B – $T_{\rm eff2} = 6630$ K) and YY evolutionary tracks for ASAS-184949 for $[M/H]$ of -0.41 (green and orange) and 0.35 (blue and red). Dashed lines represent YY isochrones calculated for a given metallicity.

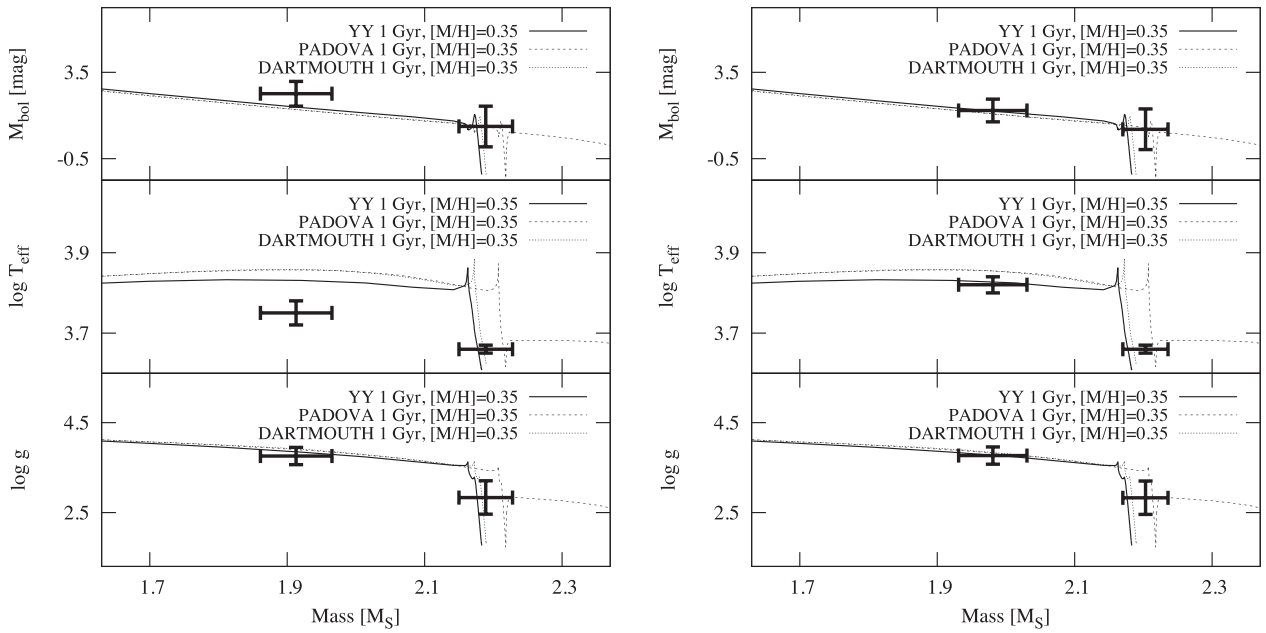

Figure 7. ASAS-184949 components parameters (left-hand panel: solution A; right-hand panel: solution B) with the best fitting YY, PARSEC, and Dartmouth isochrones of age of 1 Gyr, and metallicity $[M/H] = 0.35$.

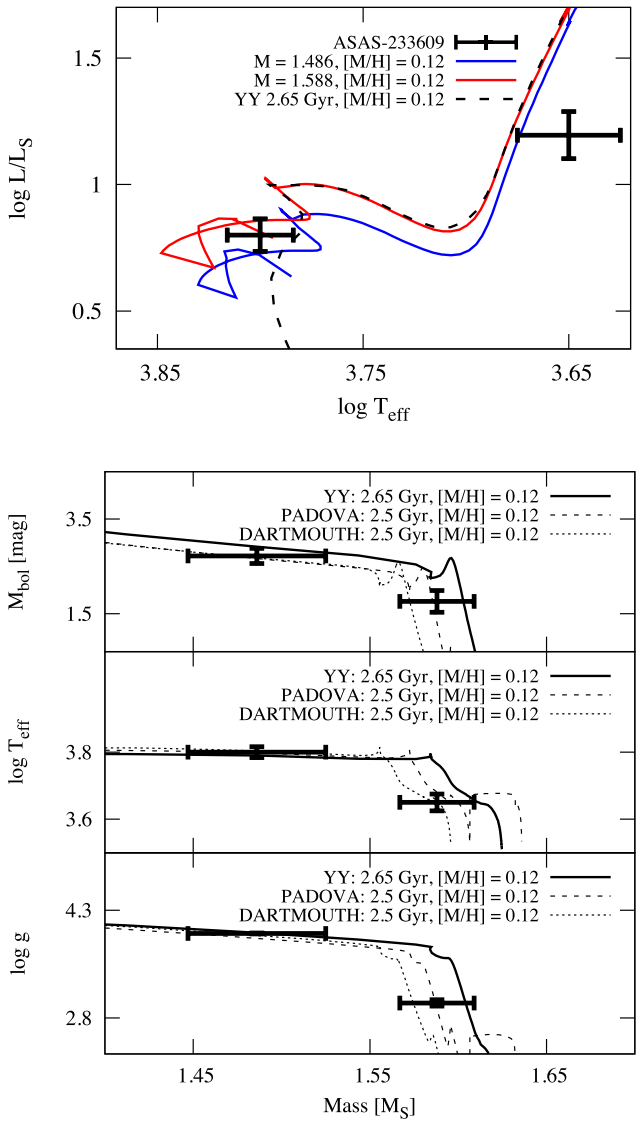

Figure 8. YY evolutionary tracks for BQ Aqr and $[M/H] = 0.12$ with corresponding isochrone (upper panel), and YY, PARSEC, and Dartmouth isochrones of age of 2.5–2.65 Gyr and $[M/H] = 0.12$ (lower panel).

Comparison of our results for V1207 Cen with YY isochones led to another inconsistency. As the SME metallicity estimation was not consistent for both components ($[M/H]_1 = -0.16$, $[M/H]_2 = -0.45$), we checked if our solution fitted evolutionary tracks calculated for both values of metallicity (left-hand panel of Fig. 9). Any pair of tracks fitted the parameters for both components equally well, offering no solution to the degeneracy in metallicity. We therefore recomputed the effective temperatures by fixing both values of metallicity (as per solution B for ASAS-184949), unfortunately with no improvement of models versus observations. In the next step, we checked if tracks calculated for a wide spread of metallicities fitted the stellar parameters. As we failed in observations and model comparison, we concluded the secondary temperature should be higher. By stepwise tweaking the secondary temperature in PHOEBE and keeping it fixed, we fitted the value of the primary one, and recalculated L and M_{bol} for both components. Such a solution was then compared with evolutionary tracks calculated for either values of metallicity $[M/H]_1 = -0.16$ and $[M/H]_2 = -0.45$. After a few iterations we found a solution consistent with the models: $T_1 = 6340$ and $T_2 = 5000$ K and the metallicity of $[M/H] = -0.45$. As shown in Fig. 9 (right-hand panel), evolutionary tracks match the redetermined parameters. However, the intersections of the tracks and the isochrone (obtained for a given metallicity and age determined from comparison presented in Fig. 10) indicates that the stellar temperatures should be similar, which is in disagreement with LC solution and unequal depths of eclipses. This discrepancy may be caused e.g. by a slightly different value of the mass ratio (within the uncertainty from RV solution presented in Table 2) than the one we obtained from our RV solution or even by the mass loss of the more evolved (secondary) component. In such a case the earlier assumption of negligible mass loss could have been invalid. Stellar parameters calculated for the new values of effective temperature are presented in Table 2 as an alternative solution after the slash. The location of the redetermined parameters on evolutionary tracks indicates differential evolutionary phases of the system components – the primary star is a subgiant, while the secondary is already at the low red giant branch.

We also compared our redetermined results with YY, PARSEC, and Dartmouth isochrones for $[M/H] = -0.45$ which yielded system ages of $\sim$ 5.7 Gyr, 4.7 Gyr, and 5.0 Gyr, respectively. The mismatch between the location of the primary star parameters on the plane of log g – mass in Fig. 10 suggests the value of log g should be lower.

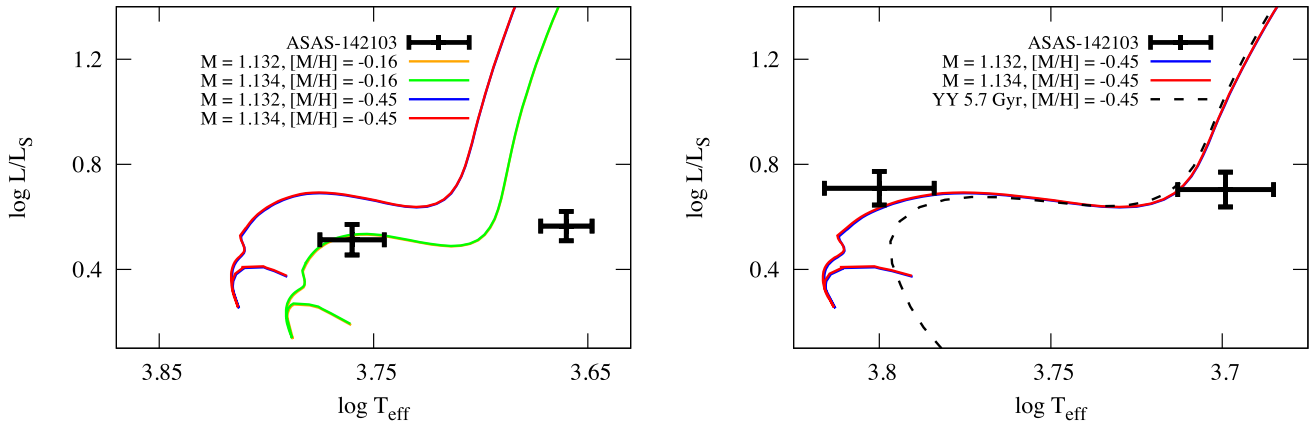

Figure 9. YY evolutionary tracks for V1207 Cen for the initial solution (left-hand panel) and the alternative one (right-hand panel).

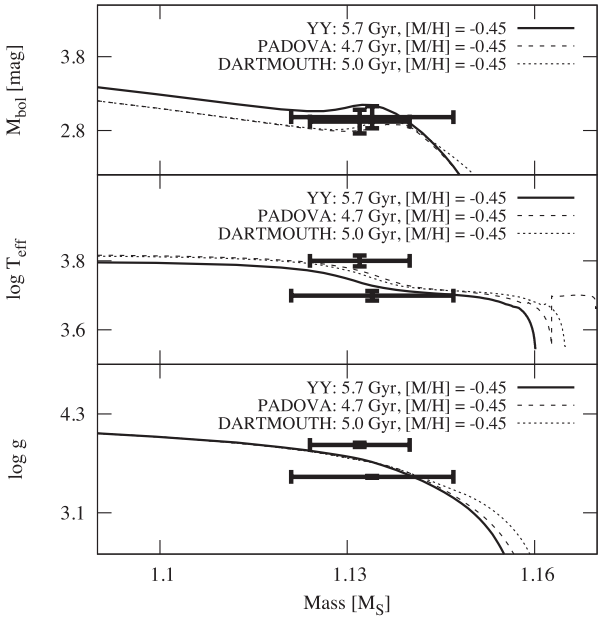

Figure 10. YY, PARSEC, and Dartmouth isochrones for $[M/H]$ of -0.45 and age of 5.7, 4.7, and 5.0 Gyr compared with V1207 Cen parameters solution.

6.2 Giants with and without spots in eclipsing binaries

In Fig. 11 we compare those eclipsing binaries with giant and subgiant components that show spots, with those that do not. Such comparisons in the literature are usually done for main-sequence stars, not giants, and using other activity indicators, like the $L_X/L_{\rm bol}$ or the calcium emission flux (R_{HK}). Numerous studies (e.g. Noyes et al. 1984; Stępień 1994; Gunn, Mitrou & Doyle 1998; Pizzolato et al. 2003; Reiners, Schüssler & Passegger 2014) relate these indicators to rotation period, as the fast rotation drives the dynamo mechanism, responsible for building strong magnetic fields, or to the Rossby number Ro – the ratio of the rotation period to the turnover time for the bottom layer convection zone τ_c (Noyes et al. 1984). Similar studies that include more evolved stars are sparse (e.g. Hall 1994; Gunn et al. 1998; Gondoin 2007). Much faster evolution after the main-sequence phase causes rapid variations in the internal structure, therefore the description of activity is more complicated than for dwarfs (Stępień 1994).

For our compilation, we selected systems from our other works, the on-line catalogue DEBCat (Southworth 2015), and also eclipsing binaries with giant and subgiant components ($R > 3$ R$_\odot$) from the Catalogue of Chromospherically Active Binary Stars (CCABS; Eker et al. 2008), for which reliable fundamental parameters can be found in the literature. Our data is not sufficient for studying $L_X/L_{\rm bol}$ or R_{HK}, therefore we use a simple photometric indicator of 'spottedness', similar to Hall (1994) or Hartman et al. (2009). As 'showing spots' we define these systems for which the spot-originated modulation is visible in ASAS LCs. Because those data are not of the best possible quality, the modulation's amplitude is typically $\gtrsim$0.1 mag in V-band. If there is no ASAS LC available, we check the literature and look for brightness variations of such a scale. The 'non-spotted' systems we have chosen typically have photometry of better quality than ASAS, and out-of-eclipse brightness fluctuations are not clearly seen.

The 'spotted' sample is built of the three targets described here, V1980 Sgr and ASAS J010538-8003.7 from Ratajczak et al. (2013),[3] and a number of so-called classical RS CVn-type stars, namely: RZ Eri, GK Hya, CF Tuc, RU Cnc, VV Mon, SS Cam, CQ Aur, SS Boo, V792 Her, SZ Psc, LX Per, and RS CVn itself.[4] Their physical and orbital parameters were taken from compilations made by Popper (1988, 1990), and supplemented by works of other authors (Imbert 1978; Arnold et al. 1979; Cerruti-Sola et al. 1980; Tümer et al. 1985; Fekel 1991; Nelson et al. 1991; Burki, Kvíz & North 1992; Eaton et al. 1993; Young 1993; Hackert & Ordway 1995; Kang et al. 2003), with the exception of CF Tuc, which analysis was revised by Dogru et al. (2009). We also added to the sample three unpublished systems we have analysed (ASAS-06, ASAS-11, ASAS-16), one of which does not have reliable temperature estimations (ASAS-16).

The 'non-spotted' sample contains 14 LMC and SMC systems (Graczyk et al. 2012; Pietrzyński et al. 2013; Pilecki et al. 2013;

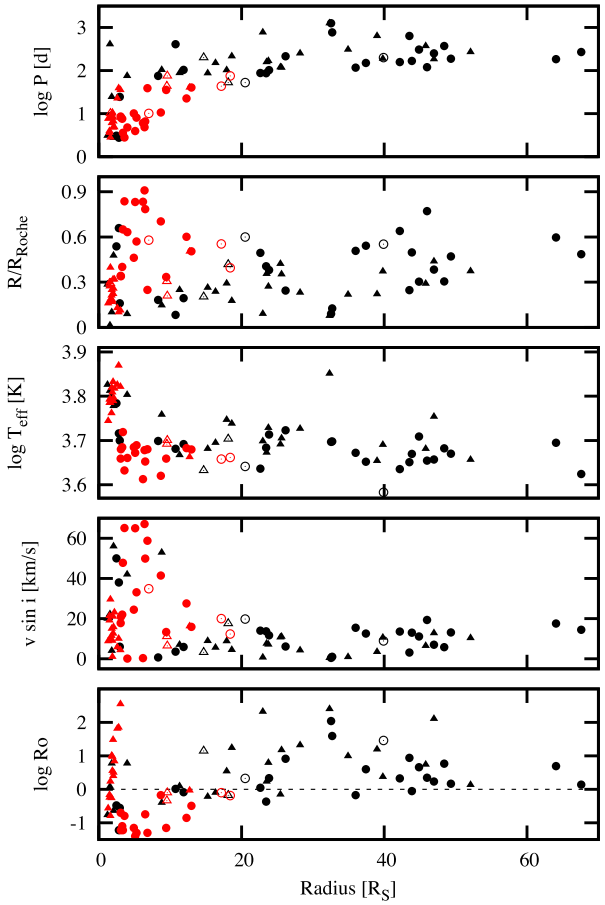

Figure 11. Comparison of eclipsing binaries with giants that also show strong spot-originated brightness modulation (red), with these that do not show it (black). Circles mark larger (usually cooler) components, and triangles the smaller (hotter) ones. Open symbols mark our unpublished systems. Orbital period P, fractional Roche lobe radius $R/R_{\rm Roche}$, effective temperature $\log(T)$, projected rotational velocity $v\sin i$, and Rossby number Ro are plotted as a function of the absolute radius. Note there are no heavily spotted giants larger than $\sim$20 R$_\odot$ and with $Ro > 1$ (marked with the dashed line).

[3] ASAS-010538 was originally considered as 'non-spotted', but a closer inspection of the ASAS LC revealed spots that clearly evolve in time.
[4] This list is incomplete, but we consider it as representative, because other RS CVn-type stars share similar characteristics, and the conclusions we present later would not change.

Graczyk et al. 2014), KIC 8410673 (Frandsen et al. 2013), AI Phe (Andersen et al. 1988; Hełminiak et al. 2009), TZ For (Andersen et al. 1991), OW Gem (Gałan et al. 2008), α Aur (Torres et al. 2009, 2015), CF Tau (Lacy, Torres & Claret 2012), V432 Aur (Siviero et al. 2014), HD187669 (Hełminiak et al. 2015), ASAS J180057-2333.8, (Suchomska et al. 2015), ASAS J182510-2435.5 (Ratajczak et al. 2013), and two more systems we have analysed but not published yet (ASAS-061, V64). We want to note, that the 'non-spotted' systems may also be active, but the activity level must be lower than for the 'spotted' ones, as there is no clear sign of variability in the published photometry, usually more precise than the ASAS data. Some of them appear in the CCABS.

In Fig. 11 we plot the orbital period, ratio of the stellar radius to the Roche radius, effective temperature, projected velocity of rotation, and Rossby number as a function of absolute radius. The Roche radius is defined as in Section 5. Rotation velocities, $v \sin i$, were either taken directly from the literature (for the non-eclipsing α Aur, it was calculated directly from the rotation periods and radii), or calculated assuming (pseudo-)synchronization,[5] which was explicitly stated in some sources. In very few cases, when no information on rotation was found, synchronization was also assumed (except the classical Cepheid in OGLE-LMC-CEP-0227, which does not appear in Fig. 11). Rossby number *Ro* values were estimated using the stellar models of Legarde et al. (2012) and τ_c values from grids calculated by the group of C. Charbonnel (private communication).

Fig. 11 shows that the 'spotted' giants reside only in relatively short-period systems, and are all smaller than 20 $R_\odot$. Through the assumption of tidal synchronization, both these facts translate into low Rossby numbers (<1) for the spotted stars, but there are a few cases of large ($R > 20\ R_\odot$) stars with equally low *Ro*. The vast majority of the spotted ones, that clusters at $R < 10\ R_\odot$ and $P < 10$ d, are the classical RS CVn-type systems. We suspect that for our objects, despite what the best-fitting solutions suggest, only the larger components truly show spots, as they are cooler than $\sim$5000 K, and rotating faster than smaller components (except for V1980 Sgr, composed of two very similar stars). They also occupy large parts of their Roche lobes. However, many 'non-spotted' systems show similar values of $R/R_{\rm Roche}$, $T_{\rm eff}$ and $v \sin i$, but are significantly larger and on long-period orbits, thus their Rossby numbers are usually higher. There are no spotted subgiants and giants (more evolved components of the systems) larger than 20 $R_\odot$ and with $Ro > 1$. The $v \sin i$ alone can not explain the existence or absence of spots, as some of the smaller spotted stars rotate with velocities between 10 and 20 km s^{-1}, as do many of the larger non-spotted objects.

The explanation for the presence or absence of spots (high and low activity) is relatively well understood, and was proposed several decades ago (Popper & Ulrich 1977). A star cools down after the main sequence, expands and becomes tidally locked, which increases the velocity of rotation. As the temperature drops, the convective envelope expands. A dynamo-like mechanism causes an increase in the magnetic field and activity, which is manifested by spots and emission lines. This is a widely-accepted scenario of the formation of active, RS CVn-type binaries (Gould et al. 2013). This is also somewhat similar to the situation of late-type dwarfs in short-period eclipsing binaries, which trapped in tidal locking, show high activity levels, and which usually exhibit significant discrepancies between observed and predicted radii and temperatures (Ribas et al. 2008).

[5] Pseudo-synchronization is a state of an equilibrium between rotation and orbital motion, achieved for non-circular orbits.

As shown by Hall (1991, 1994), larger, spot-originated brightness variability of dwarfs is correlated with lower values of *Ro*. He found a threshold at $R \simeq 0.65$ between photometrically stable and variable stars. A similar situation can be seen in Fig. 11, where we arbitrarily set the threshold at $Ro \simeq 1$ ($P_{\rm rot} \simeq \tau_c$), but only for stars smaller than 20 $R_\odot$.

We conclude that the activity in giants and subgiants seems to be working in a similar way as in dwarfs, where it is most likely driven by some form of dynamo mechanism (Feiden & Chaboyer 2012, 2013). We can thus suspect that highly active giants may exhibit similar discrepancies to the dwarfs when compared to evolutionary models, i.e. oversized radii and lower effective temperatures (Ribas et al. 2008; Hełminiak & Konacki 2011). The difference is that giants larger than 20 $R_\odot$ tend to be less active, despite having other parameters ($v \sin i$, *Ro*) which are similar to those for the smaller and active ones, suggesting that the size or internal structure plays role in sustaining or suppressing the activity. On the other hand, as pointed out by Stępień (1994), giants' activity may be more complicated, taking into account relatively rapid changes in their internal structure, but the cut-off in radii seems to be real. It is important to emphasize the criterion we have used to distinguish between active (spotted) and less-active (non-spotted) stars is not very robust, and stars we marked as 'non-spotted' sometimes show other signs of activity. For a more complete picture of red giants' activity, additional active, evolved systems should be identified and studied. Optimally, cases of spotted and non-spotted, short-period, large and very large ($>20\ R_\odot$) giants should be observed, to investigate if high *Ro* and *R* are the only factors that suppress the activity in evolved stars. Further observations, and measurements of the intensity of magnetic fields should also be done, and would probably help to determine which kind of dynamo mechanism works in giant, and presumably in dwarf stars.

7 CONCLUSIONS

RV curves and full sets of orbital and physical parameters for three DEB systems (ASAS-184949, BQ Aqr, and V1207 Cen) are presented for the first time. For BQ Aqr and V1207 Cen we obtained masses and radii values with uncertainties of 1–2 and 2–4 per cent, respectively. Such precision could make these systems useful test beds for empirical verification of stellar evolution models. Despite this high precision, finding a consistent solution for V1207 Cen proved non-trivial. Due to the lack of WASP photometry, the radii in ASAS-184949 are determined to only 20–40 per cent, but mass errors are of $\sim$ 2–4 per cent.

The efficient phase coverage of the RVs made it possible to apply spectral disentangling and spectral analysis yielding independently effective temperatures, and metallicities of the systems' components. As we found inconsistent metallicities for the two components, we decided not to perform an analysis of the chemical abundances.

All three systems we analysed consist of a red giant and a less evolved star (in a main-sequence or a subgiant phase). Well-characterized detached systems which have not undergone mass transfer, and which consist of components in a slightly different degree of evolution are not very common (Southworth 2015). Fitting models of the same age to the observed properties of both components provides a very stringent test of the models, therefore all of the systems constitute very informative objects worthy of more detailed analysis.

Chromospheric activity of the systems' components, manifested in the existence of spots, is significant for every single system we

analysed. Activity is clearly visible in the spectra of A184949 and V1207 Cen, as well as in the shape of the cross-correlation function of BQ Aqr, and causes time-varying LC variations in every system. Applying models with spots reproduced the photometric measurements with great performance. Taking into account the stellar parameters and activity of the analysed objects, they can be also classified as classical RS CVn stars (Hall 1976).

By comparing the properties of giants with and without spots, we found a hint of an activity cut-off at $Ro \sim 1$, and $R \sim 20$ $R_{\odot}$. Nevertheless, the details of processes responsible for induction and suppression of stellar activity are still an open question. If the activity observed in the studied systems is induced by rotation and tidal locking, as in dwarfs, further observations of new active, evolved systems might help to distinguish which dynamo mechanism is responsible for the enhanced stellar activity, and resolve the discrepancies between observed and theoretically predicted fundamental stellar parameters.

During the analysis we found several issues troublesome. Metallicities derived from spectral analysis are inconsistent between the two components of ASAS-184949 and do not agree with evolutionary tracks for given masses. Also, the temperature determination is particularly unsatisfactory (solution A for ASAS-184949, V1207 Cen). The obvious complication in determining the temperature are evolving spots, which change the stellar temperature as the star rotates. Spots also affect the outcome of spectral disentangling, as a final decomposed spectrum of a single star is a product of averaging spectra taken with spots visible from different angles.

Another reason for the inconsistencies we met is the brightness ratio, which – due to the spots' existence – is not trivial to determine from LC even for systems with total eclipses (spots cause changes in eclipse depths, so it is not easy to determine the exact decrease of total brightness). Thus in the modelling we performed, we took the *BR* value from the TODCOR analysis (which was consistent with the LC-based *BR* for the base season without spots). This value was used to scale the disentangled spectra, therefore the entire spectral analysis was based on it.

The analyses we carried out for BQ Aqr and V1207 Cen enrich a relatively small sample of well-characterized red giants, and systems with components in slightly different phases of evolution. In order to improve the radii determination for ASAS-184949, more precise photometry is required. Multicolour photometry for all three systems would be useful to study evolving spots and improve stellar temperature estimation. Infrared observations (both photometric and spectroscopic) could both enrich the study of spots, and allow the investigation of a spectral region where more chromospheric activity indicators are hidden.

ACKNOWLEDGEMENTS

This article is based on observations collected through CNTAC proposals CN-2012A-21, CN-2012B-36, CN-2013A-93, CN-2013B-22, CN- 2014A-044 and CN-2014B-067, at the European Southern Observatory, Chile under programmes 089.D-0097 and 091.D-0145, and at the Subaru Telescope, which is operated by the National Astronomical Observatory of Japan, via the time exchange programme between Subaru and the Gemini Observatory. The authors would like to thank M. Armano from ESA for valuable comments, the group of C. Charbonnel from Geneva Observatory for sharing their grids, and the referee for constructive suggestions which helped to improve the manuscript.

This work is supported by the National Science Center through grants 2011/01/N/ST9/02209 (MR), 5813/B/H03/2011/40 (MK), and 2011/03/B/ST9/01819 (KGH), by the European Research Council through a Starting Grant, and by the Foundation for Polish Science through 'Idee dla Polski' funding scheme. KGH acknowledges support provided by the National Observatory of Japan as Subaru Astronomical Research Fellow.

This research has made use of the Simbad data base, operated at CDS, Strasbourg, France.

The authors wish to recognize and acknowledge the very significant cultural role and reverence that the summit of Mauna Kea has always had within the indigenous Hawaiian community. We are most fortunate to have the opportunity to conduct observations from this mountain.

REFERENCES

Andersen J., Clausen J. V., Nordstrorm B., Gustafsson B., Vandenberg D. A., 1988, A&A, 196, 128
Andersen J., Clausen J. V., Nordstorm B., Tomkin J., Mayor M., 1991, A&A, 246, 99
Arnold C. N., Montle R. E., Stuhlinger T. W., Hall D. S., 1979, Acta Astron., 29, 243
Bagnuolo W. G., Gies D. R., 1991, ApJ, 376, 266
Bessell M. S., Castelli F., Plez B., 1998, A&A, 333, 231
Bressan A., Marigo P., Girardi L., Salasnich B., Dal Cero C., Rubele S., Nanni S., 2012, MNRAS, 427, 127
Burki G., Kvíz Z., North P., 1992, A&A, 256, 463
Cerruti-Sola M. et al., 1980, A&A, 42, 245
Dogru D., Erdem A., Dogru S. S., Zola S., 2009, MNRAS, 397, 1647
Dotter A., Chaboyer B., Jevremovic D., Baron E., Ferguson J. W., Sarajedini A., Anderson J., 2007, AJ, 134, 376
Eaton J. A., Henry G. W., Bell C., Okorogu A., 1993, AJ, 106, 1181
Eggleton P. P., 1983, ApJ, 268, 368
Eker Z. et al., 2008, MNRAS, 389, 1722
Feiden G. A., Chaboyer B., 2012, ApJ, 761, 30
Feiden G. A., Chaboyer B., 2013, ApJ, 779, 183
Fekel F. C., 1991, AJ, 101, 1489
Frandsen S. et al., 2013, A&A, 556, A138
Gałan C., Mikołajewski M., Tomov T., Kolev D., Graczyk D., Majcher A., Janowski J. L., Cikala M., 2008, Observatory, 128, 298
Gondoin P., 2007, A&A, 464, 1101
Gould A. et al., 2013, ApJ, 763, 141
Graczyk D. et al., 2012, ApJ, 750, 144
Graczyk D. et al., 2014, ApJ, 780, 59
Grevesse N., Asplund M., Sauval A. J., 2007, Space Sci. Rev, 130, 105
Gunn A. G., Mitrou C. K., Doyle J. G., 1998, MNRAS, 296, 150
Hall D. S., 1976, Astrophys. Space. Sci. Lib., 60, 287
Hall D. S., 1991, in Tuominen I., Moss D., Rüdiger G., eds, The Sun and Cool Stars: Activity, Magnetism, Dynamos. Springer Verlag, Berlin, p. 353
Hall D. S., 1994, Mem. Soc. Astron. Ital., 65, 73
Hartmann J. D. et al., 2009, ApJ, 691, 342
Heckert P. A., Ordway J. I., 1995, AJ, 109, 2169
Hełminiak K. G., Konacki M., 2011, A&A, 526, A29
Hełminiak K. G., Konacki M., Muterspaugh M. W., Ratajczak M., 2009, MNRAS, 400, 969
Hełminiak K. G., Brahm R., Ratajczak M., Espinoza N., Jordan A., Konacki M., Rabus M., 2014, A&A, 567, 64
Hełminiak K. G. et al., 2015, MNRAS, 448, 1945
Hoffmeister C., 1931, Astron. Nachr., 242, 129
Høg E. et al., 2000, A&A, 355, 27
Ilijic S., Hensberge H., Pavlovski K., Freyhammer L., 2004, ASP Conf. Ser. Vol. 318, Spectroscopically and Spatially Resolving the Components of Close Binary Stars. Astron. Soc. Pac., San Francisco, p. 111
Imbert M., 1978, A&AS, 33, 321
Jordan A. et al., 2014, AJ, 148, 29
Kang Y. W., Lee W.-B., Kim H.-I., Oh K.-D., 2003, MNRAS, 344, 1227

Kaufer A. et al., 1999, The Messenger, 95, 8
Klinglesmith D. A., Sobieski S., 1970, AJ, 75, 175
Konacki M., Muterspaugh M. W., Kulkarni S. R., Hełminiak K. G., 2010, ApJ, 719, 129
Kordopatis G. et al., 2013, AJ, 146, 134
Kupka F., Piskunov N., Ryabchikova T. A., Stempels H. C., Weiss W. W., 1999, A&AS, 138, 119
Lacy C. H. S., Torres G., Claret A., 2012, AJ, 144, 167
Lastennet E., Vall-Gabaud D., 2002, A&A, 396, 551
Legarde N., Decressin T., Charbonnel C., Eggenberger P., Ekstrom S, Palacios A., 2012, A&A, 543, 108
Lucy L. B, 1967, Z. Astrophys., 65, 98
Nelson C. H., Hall D. S., Fekel F. C., Fried R. E., Lines R. E., Lines H. C., 1991, Ap&SS, 182, 1
Noguhi K. et al., 2002, PASJ, 54, 855
Noyes R. W., Hartmann L. W., Baliunas S. L., Duncan D. K., Vaughan A. H., 1984, ApJ, 279, 763
Pietrzyński G. et al., 2013, Nature, 495, 76
Pilecki B. et al., 2013, MNRAS, 436, 953
Piskunov N., Kupka F., Ryabchikova T. A, Weiss W. W., Jeffery C. S., 1995, A &AS, 112, 525
Pizzolato N., Maggio A., Micela G., Sciortino S., Ventura P., 2003, A&A, 397, 147
Pojmański G., 2002, Acta Astron., 52, 397
Pollacco D. L. et al., 2006, PASP, 118, 1407
Popper D. M., 1988, AJ, 96, 1040
Popper D. M., 1990, AJ, 100, 247
Popper D. M., Ulrich R. K., 1977, ApJ, 212, L131
Prša A., Zwitter T., 2005, ApJ, 628, 426
Queloz D. et al., 2001, The Messenger, 105, 1
Ratajczak M., Hełminiak K. G., Konacki M., Jordan A., 2013, MNRAS, 433, 2357
Reiners A., Schüssler M., Passegger V. M., 2014, ApJ, 794, 144
Ribas I., Morales J. C., Jordi C., Baraffe I., Chabrier G., Gallardo J., 2008, Mem. Soc. Astron. Ital., 79, 562
Schlafly E. F., Finkbeiner D. P., 2011, ApJ, 737, 103
Schlegel D., Finkbeiner D., Davis M., 1998, ApJ, 500, 525
Schroder K. P., Cuntz M., 2005, ApJ, 630, 73
Schwab Ch., Spronck J., Tokovinin A., Szymkowiak A., Giguere M., Fisher D., 2012, in McLean I. S., Ramsay S. K., Takami H., eds, Proc. SPIE Conf. Ser. Vol. 8446, Performance of the CHIRON High-Resolution Echelle Spectrograph. SPIE, Bellingham, p. 16
Sitek M., Pojmański G., 2014, Acta Astron., 64, 115
Siviero A., Munari U., Sordo R., Dallaporta S., Marrese P. M., Zwitter T., Milone E. F., 2014, A&A, 417, 1083
Smith A. M. S. et al., 2006, MNRAS, 373, 1151
Southworth J., 2015, ASP Conf. Ser., 466, 164
Southworth J., Maxted P. F. L., Smalley B., 2004a, MNRAS, 351, 1277
Southworth J., Zucker S., Maxted P. F. L., Smalley B., 2004b, MNRAS, 355, 986
Strassmeier K. G., Handler G., Pauzen E., Raith M., 1993, A&A, 281, 855
Strohmeier W., 1966, Inf. Bull. Var. Stars, 158, 1
Stępień K., 1994, A&A, 292, 191
Suchomska K. et al., 2015, MNRAS, 451, 651
Tamuz O., Mazeh T., Zucker S., 2005, MNRAS, 356, 1466
Tokovinin A. et al., 2013, PASP, 125, 1336
Torres C. A. O., Quast G. R., Da Silva L., De Le Reza R., Melo C. H. F., Sterzik M., 2006, A&A, 460, 695
Torres G., Claret A., Young P. A., 2009, ApJ, 700, 1349
Torres G., Andersen J., Gimenéz A., 2010, A&AR, 18, 67
Torres G., Claret A., Pavlovski K., Dotter A., 2015, ApJ, 807, 26
Tümer O., Ibanoğlu C., Evren S., Tunca Z., 1985, Ap&SS, 112, 273
Valenti J. A., Fischer D. A., 2005, ApJS, 159, 141
Valenti J. A., Piskunov N., 1996, A&AS, 118, 595
Valenti J. A., Piskunov N., Johns-Krull C. M., 1998, ApJ, 498, 851
van Hamme W., 1993, AJ, 106, 2096
Voges W. et al., 1999, A &A, 349, 389
Worthey G., Lee H., 2011, ApJ, 193, 1
Yi S. K., Demarque P., Kim Y. C., Lee Y. W., Ree C. H., Lejeune T., Barnes S., 2001, ApJS, 136, 417
Young W. K., 1993, Ap&SS, 201, 35
Zucker S., Mazeh T., 1994, ApJ, 420, 806

APPENDIX: RV MEASUREMENTS FOR ASAS-184949, BQ AQR, AND V1207 CEN SYSTEMS

The section includes Tables A1–A3 with RV measurements, formal RV errors, O-Cs, exposure times for each spectrum, SNR and telescope specifications for both components of the selected systems. The used telescopes/spectrographs are as follows: CTIO/CH = CTIO 1.5-m/CHIRON(f – fibre mode, s – slicer mode) EUL/C = Euler/CORALIE, SUB/HDS = Subaru/HDS (red or blue CCD chip), ESO/F = MPG/ESO 2.2-m/FEROS. SNR stands for a signal-to-noise ratio per collapsed spectral pixel at $\lambda = 5500$ Å, except HDS red chip ($\lambda = 6070$ Å) and HDS blue chip ($\lambda = 4760$ Å) measurements.

Table A1. RV measurements for ASAS-184949.

BJD-2450000	RV_1 [km s^{-1}]	σ_{RV_1} [km s^{-1}]	$O-C_1$ [km s^{-1}]	RV_2 [km s^{-1}]	σ_{RV_2} [km s^{-1}]	$O-C_2$ [km s^{-1}]	T_{exp} [s]	SNR	Tel./Sp.
5778.82120	−7.5	1.3	3.1	26.5	1.4	−0.8	600	71	SUB/HDS red
5778.82120	−9.2	1.8	1.4	27.6	2.4	0.3	600	55	SUB/HDS blue
5855.70366	−46.6	0.8	−0.9	59.0	1.6	1.0	600	110	SUB/HDS red
5855.70366	−45.9	0.6	0.3	58.1	2.3	0.1	600	100	SUB/HDS blue
6084.67520	42.6	1.5	0.3	−24.6	11.0	2.0	660	28	EUL/C
6085.69223	49.2	1.1	0.3	−34.4	7.0	−2.0	660	32	EUL/C

Table A1 – *continued*

BJD-2450000	RV_1 [km s^{-1}]	σ_{RV_1} [km s^{-1}]	$O-C_1$ [km s^{-1}]	RV_2 [km s^{-1}]	σ_{RV_2} [km s^{-1}]	$O-C_2$ [km s^{-1}]	T_{exp} [s]	SNR	Tel./Sp.
6102.72019	−31.8	0.5	0.4	42.2	1.3	1.6	600	80	ESO/F
6178.16692	−48.9	3.0	0.7	55.0	3.0	1.2	720	10	EUL/C
6179.09118	−48.5	1.4	1.2	56.1	4.0	2.2	660	25	EUL/C
6195.08229	60.1	0.8	0.6	−45.6	9.0	−6.0	720	90	ESO/F
6397.75597	−30.8	1.6	0.4	36.5	8.0	−1.1	900	31	EUL/C
6398.83712	−21.7	1.3	0.4	28.3	1.9	−1.9	900	28	EUL/C
6428.69235	−49.1	0.8	−0.3	56.5	3.0	1.4	600	53	ESO/F
6497.78145	−47.5	0.9	−1.9	48.7	2.4	−1.4	900	24	EUL/C
6498.63918	−47.7	1.1	0.4	54.8	1.9	2.3	900	29	EUL/C
6506.77702	−13.2	1.4	2.2	25.9	1.4	−1.6	700	50	CTIO/CH f
6512.67112	38.7	1.1	0.0	−21.3	3.0	−1.6	700	50	CTIO/CH f
6515.71922	56.7	0.7	0.2	−36.4	2.7	−1.1	700	50	CTIO/CH f
6517.66739	60.5	0.9	0.0	−40.3	6.0	−1.5	700	50	CTIO/CH f
6517.68720	60.4	1.0	−0.8	−43.3	8.0	−2.1	720	41	ESO/F
6519.71238	57.8	0.9	−0.7	−42.8	4.0	−4.0	600	63	ESO/F
6519.72110	57.8	0.8	−0.7	−42.4	2.2	−4.0	500	55	ESO/F
6522.65524	42.6	0.9	0.3	−21.4	0.6	1.6	700	50	CTIO/CH f
6532.64753	−41.5	1.9	−0.1	49.0	1.4	−1.4	700	50	CTIO/CH f
6547.53627	31.4	0.8	−0.5	−14.6	2.2	−0.9	700	50	CTIO/CH f
6554.53677	60.1	1.0	0.3	−42.7	8.0	−4.5	700	50	CTIO/CH f
6555.53447	57.7	0.8	−0.5	−41.0	2.0	−4.9	700	50	CTIO/CH f
6577.51728	−21.0	1.7	0.3	30.2	2.2	−2.6	700	50	CTIO/CH f
6582.50199	22.7	2.5	−2.6	−8.6	2.5	0.6	700	50	CTIO/CH f
6582.53138	21.8	1.7	−3.9	−10.1	3.0	−1.8	700	50	CTIO/CH f
6584.51811	41.2	2.4	−0.8	−24.8	3.0	−2.2	700	50	CTIO/CH f

Table A2. RV measurements for BQ Aqr.

BJD-2450000	RV_1 [km s^{-1}]	σ_{RV_1} [km s^{-1}]	$O-C_1$ [km s^{-1}]	RV_2 [km s^{-1}]	σ_{RV_2} [km s^{-1}]	$O-C_2$ [km s^{-1}]	T_{exp} [s]	SNR	Tel./Sp.
5846.71804	−53.6	0.8	0.0	86.3	9.0	−2.4	750	20	EUL/C
5893.55044	−26.1	0.5	0.1	65.9	6.0	3.6	960	13	CTIO/CH s
6079.92999	52.3	0.3	0.3	−6.9	9.0	4.0	1270	20	CTIO/CH s
6080.92988	101.9	1.4	−0.3	−50.9	10.0	6.2	750	13	EUL/C
6081.86515	86.1	0.6	−0.9	−34.1	6.0	8.1	750	23	EUL/C
6083.93994	−56.2	0.4	−0.7	86.3	6.0	−3.4	1270	26	CTIO/CH s
6084.88699	−59.2	0.3	0.4	95.9	6.0	1.6	900	24	EUL/C
6179.72531	84.2	0.4	0.3	−40.7	5.0	−0.7	900	25	EUL/C
6180.78603	99.9	0.4	−0.6	−50.9	7.0	4.7	900	28	EUL/C
6192.74475	70.9	0.3	0.1	−29.3	3.0	−0.9	1200	27	CTIO/CH s
6242.64302	−47.6	0.6	−0.7	83.8	6.0	1.4	900	30	EUL/C
6497.72638	94.1	0.6	0.1	−54.2	6.0	−4.7	900	22	EUL/C
6497.89228	99.4	0.3	−0.1	−57.3	3.0	−2.8	900	31	EUL/C
6498.84591	91.2	0.4	0.2	−41.6	12.0	5.0	900	24	EUL/C
6506.89276	−10.4	0.3	−0.1	39.7	3.0	−6.3	750	45	CTIO/CH f
6508.93344	-45.5	0.2	−0.0	85.1	5.0	6.3	750	45	CTIO/CH f
6512.72126	51.9	0.4	−0.2	−9.8	5.0	2.7	750	45	CTIO/CH f
6514.84285	-66.2	0.3	0.07	95.4	3.0	−2.8	750	45	CTIO/CH f
6538.75587	82.0	0.3	0.6	−40.4	8.0	−0.4	750	40	CTIO/CH f
6547.84414	-66.3	0.3	−0.1	92.0	4.0	−6.2	750	40	CTIO/CH f
6550.65153	91.9	0.4	−0.4	−52.8	3.0	−2.8	750	35	CTIO/CH f
6556.54973	47.4	0.4	−0.9	−5.4	3.0	3.6	750	45	CTIO/CH f
6568.51741	-44.9	0.4	−0.9	88.4	5.0	9.7	750	40	CTIO/CH f
6570.61228	95.9	0.3	−0.1	−52.4	3.0	−2.7	750	40	CTIO/CH f
6575.52576	−20.6	0.8	0.4	45.5	6.0	−10.4	750	30	CTIO/CH f
6581.52829	−56.0	0.5	−0.1	93.6	2.8	4.9	750	35	CTIO/CH f
6583.53373	81.5	0.5	−0.2	−43.9	6.0	−3.8	750	35	CTIO/CH f

Table A3. RV measurements for V1207 Cen.

BJD-2450000	RV_1 [km s^{-1}]	σ_{RV_1} [km s^{-1}]	$O-C_1$ [km s^{-1}]	RV_2 [km s^{-1}]	σ_{RV_2} [km s^{-1}]	$O-C_2$ [km s^{-1}]	T_{exp} [s]	SNR	Tel./Sp.
6692.88109	−6.3	0.2	0.0	−142.6	0.8	−0.7	900	50	CTIO/CH f
6736.65885	−26.9	0.2	0.3	−120.4	1.0	0.6	900	50	CTIO/CH f
6749.69003	−113.1	0.2	0.1	−33.9	0.8	0.9	900	50	CTIO/CH f
6769.67348	−6.4	0.2	−0.0	−140.8	0.8	1.1	900	50	CTIO/CH f
6790.56491	−138.8	0.3	−0.3	−9.8	0.7	−0.3	900	50	CTIO/CH f
6840.58050	−96.2	0.3	0.0	−51.7	0.7	0.1	900	50	CTIO/CH f
6869.52784	−98.4	0.7	0.6	−50.7	1.8	−1.6	900	50	CTIO/CH f
6898.49168	−15.9	0.2	−0.2	−133.1	1.3	−0.6	1000	60	CTIO/CH f
6904.49056	−58.8	0.1	−0.1	−90.2	0.6	−0.7	1000	60	CTIO/CH f

This paper has been typeset from a TEX/LATEX file prepared by the author.